

RESEARCH ARTICLE

Non-water-suppressed short-echo-time magnetic resonance spectroscopic imaging using a concentric ring *k*-space trajectoryUzay E. Emir¹  | Brian Burns² | Mark Chiew¹ | Peter Jezzard¹ | M. Albert Thomas³¹FMRIB Centre, Nuffield Department of Clinical Neurosciences, University of Oxford, John Radcliffe Hospital, Oxford, UK²Department of Oncology, University of Oxford, Oxford, UK³Department of Radiological Sciences, University of California, Los Angeles, CA, USA

Correspondence

Uzay E. Emir, FMRIB Centre, Nuffield Department of Clinical Neurosciences, University of Oxford, John Radcliffe Hospital, Oxford, UK.
Email: uzay.emir@ndcn.ox.ac.uk

Water-suppressed MRS acquisition techniques have been the standard MRS approach used in research and for clinical scanning to date. The acquisition of a non-water-suppressed MRS spectrum is used for artefact correction, reconstruction of phased-array coil data and metabolite quantification. Here, a two-scan metabolite-cycling magnetic resonance spectroscopic imaging (MRSI) scheme that does not use water suppression is demonstrated and evaluated. Specifically, the feasibility of acquiring and quantifying short-echo ($T_E = 14$ ms), two-dimensional stimulated echo acquisition mode (STEAM) MRSI spectra in the motor cortex is demonstrated on a 3 T MRI system. The increase in measurement time from the metabolite-cycling is counterbalanced by a time-efficient concentric ring *k*-space trajectory. To validate the technique, water-suppressed MRSI acquisitions were also performed for comparison. The proposed non-water-suppressed metabolite-cycling MRSI technique was tested for detection and correction of resonance frequency drifts due to subject motion and/or hardware instability, and the feasibility of high-resolution metabolic mapping over a whole brain slice was assessed. Our results show that the metabolite spectra and estimated concentrations are in agreement between non-water-suppressed and water-suppressed techniques. The achieved spectral quality, signal-to-noise ratio (SNR) > 20 and linewidth < 7 Hz allowed reliable metabolic mapping of five major brain metabolites in the motor cortex with an in-plane resolution of 10×10 mm² in 8 min and with a Cramér-Rao lower bound of less than 20% using LCModel analysis. In addition, the high SNR of the water peak of the non-water-suppressed technique enabled voxel-wise single-scan frequency, phase and eddy current correction. These findings demonstrate that our non-water-suppressed metabolite-cycling MRSI technique can perform robustly on 3 T MRI systems and within a clinically feasible acquisition time.

KEYWORDS

concentric rings, metabolite-cycling, non-water-suppressed, spectroscopic imaging

Abbreviations used: 2D, two dimensional; Cho, choline; Cr, creatine; CRLB, Cramér-Rao lower bound; EPSI, echo-planar spectroscopic imaging; FFT, fast Fourier transform; FOV, field of view; GABA, γ -aminobutyric acid; Gln, glutamine; Glu, glutamate; GM, grey matter; GPC, glycerophosphocholine; HLSVD, Hankel-Lanczos singular value decomposition; Lac, lactate; MRSI, magnetic resonance spectroscopic imaging; *myo*-Ins, *myo*-inositol; NAA, N-acetylaspartate; NUFFT, non-uniform FFT; OVS, outer volume suppression; PE, phosphoethanolamine; SAR, specific absorption rate; SD, standard deviation; SNR, signal-to-noise ratio; STEAM, stimulated echo acquisition mode; SV, single voxel; tCho, total choline; tCr, total creatine; tNAA, total N-acetylaspartate; VAPOR, variable-power RF pulses with optimized relaxation delays; VOI, volume of interest; WM, white matter

1 | INTRODUCTION

Non-invasive measurement of metabolite concentrations by proton MRS is of great potential value for studying the metabolic state of healthy and diseased brains.¹ For example, MRS allows detection of a variety of neurochemicals, including N-acetylaspartate (NAA) as a marker of neuronal loss/dysfunction, creatine (Cr) as a marker for deficits in energy metabolism, choline (Cho) as a marker for cell membrane turnover, glutamate (Glu) as the primary excitatory neurotransmitter and γ -aminobutyric acid (GABA) as the primary inhibitory neurotransmitter. Thus, MRS can contribute not only to the diagnosis and

This is an open access article under the terms of the Creative Commons Attribution License, which permits use, distribution and reproduction in any medium, provided the original work is properly cited.

© 2017 The Authors. *NMR in Biomedicine* published by John Wiley & Sons Ltd.

monitoring of disease,¹ but also to the measurement of modulations in functional neurochemistry during physiological interventions.² For example, the detection of NAA and GABA has been valuable in helping to understand neuropathological and biochemical abnormalities in neurodegenerative diseases such as amyotrophic lateral sclerosis³ and Parkinson's disease.⁴ In addition, non-invasive detection of the oncometabolite 2-hydroxyglutarate in brain tumours using MRS has the potential to be an imaging biomarker to monitor disease progression and response to therapy.^{5–7}

MRS data can be obtained either from a single voxel (SV-MRS), albeit limited to a small volume of interest (VOI), or from multiple voxels (magnetic resonance spectroscopic imaging, MRSI), which acquires metabolic profiles over larger regions of the brain. However, compared with SV-MRS, the use of MRSI has been limited by several challenges, such as inhomogeneity of the main (B_0) and RF magnetic fields, long acquisition times, insufficient water suppression, eddy-current-induced gradient errors, and line broadening artefacts caused by subject motion and scanner instability.¹

In order to separate metabolite signals from abundant water signal robustly, *in vivo* MRS methods require techniques for suppression of the water signal during acquisition^{8–11} and/or post-processing.¹² The vendor-provided MRS packages on clinical scanners offer water-suppressed spectroscopic acquisition techniques as the standard approach.¹³ However, the acquisition of a non-water-suppressed MRS spectrum is generally required to act as an internal reference for metabolite quantification. This information can also be required for optimal reconstruction of spectra from different phased-array coils, the correction of gradient-induced sideband modulations, eddy-current-induced artefacts and tracking B_0 drifts due to subject motion or scanner drift. Although numerically optimized water suppression techniques are available,⁹ vendor-provided MRS packages on clinical scanners are not fully optimized and result in, for example, baseline distortions due to poor water suppression. The recent advances in MRI hardware, especially the increase in the effective dynamic range of the analogue-to-digital converter (>12 bit), enable us to acquire water and metabolite signals simultaneously. Thus, *in vivo* MRS techniques (and particularly MRSI) that do not require water suppression^{12–18} can address this problem by eliminating the requirement for the water suppression whilst inherently providing acquisition of the water reference spectra.

In recent years, fast k -space trajectories, both echo-planar (echo-planar spectroscopic imaging or EPSI¹⁹) and non-echo-planar (spiral,²⁰ rosette²¹ and concentric^{22–24} spectroscopic imaging), have been developed to reduce the number of required phase encoding steps and, therefore, the acquisition time. It has been demonstrated that MRSI using an EPSI trajectory enables 3D metabolite mapping with whole brain coverage within clinically acceptable acquisition times.^{25–27} Although EPSI reduces acquisition duration in one spatial direction, it still suffers from relatively long scan times due to the number of required phase encoding steps. Alternatively, spiral and rosette k -space trajectories offer reduced acquisition duration for MRSI but suffer from discrepancies between their desired and true trajectories due to system imperfections (such as gradient timing delays and eddy currents). The concentric rings trajectory, which uses concentrically circular trajectories, is time efficient compared with

EPSI and is less sensitive to system imperfections compared with spiral MRSI.²² However, non-uniform k -space sampling results in signal-to-noise ratio (SNR) loss.²²

The intent of this work, therefore, is to develop a non-water-suppressed MRSI acquisition technique that addresses the challenges of sensitivity, spectral quality, speed and spatial resolution whilst also providing the required information for voxel-wise single-scan frequency, phase, gradient-induced sideband and eddy current correction. To achieve this, a non-water-suppressed metabolite-cycling two-dimensional (2D) MRSI acquisition technique with asymmetric narrow-transition-band adiabatic inversion pulses^{14–16} is proposed for simultaneous detection of the metabolites and water signals at short echo time ($T_E = 14$ ms) using stimulated echo acquisition mode (STEAM) localization. Even though a major drawback of this method is due to the doubling of the measurement time by the metabolite-cycling, it is counterbalanced by a time efficient concentric ring k -space trajectory. To validate metabolite profiles obtained using the newly developed acquisition technique, we compare profiles quantified from non-water-suppressed and conventionally water-suppressed STEAM MRSI scans acquired from the motor cortex.

2 | METHODS

Five healthy volunteers (three males/two females, aged 28.8 ± 3.4 (mean \pm sd) years) participated in this study after giving informed consent under an institutionally approved technical development protocol.

2.1 | MRI data acquisition

All scans were acquired using a Siemens Prisma 3-Tesla (Siemens, Erlangen, Germany) whole body MRI scanner (with a maximum gradient of 80 mT/m and maximum slew rate of 200 mT/m/ms) and a 32-channel (N_{cha}) head array receive coil. A high-resolution T_1 -weighted MP-RAGE dataset ($T_R = 1900$ ms, $T_E = 3.97$ ms, $T_1 = 904$ ms, flip angle $= 8^\circ$, 192 transverse slices, 1 mm³ isotropic voxels) was also acquired for accurate MRSI grid placement. B_0 shimming was achieved using GRESHIM (gradient-echo shimming).²⁸

2.2 | MRSI data acquisition

2.2.1 | Non-water-suppressed metabolite-cycling MRSI

The non-water-suppressed metabolite-cycling MRSI acquisition was achieved by utilizing two asymmetric narrow-transition-band adiabatic RF pulses with mirrored inversion profiles applied in alternate scans for the inversion of the upfield and downfield (relative to water) spectral resonances before the STEAM localization with a gap of 9.6 ms.¹⁴ Using a maximum B_1 of 19 μ T and pulse duration (T_p) of 27 ms, an 80 Hz transition bandwidth ($-0.95 < M_z/M_0 < 0.95$) and 820 Hz inversion bandwidth ($-1 < M_z/M_0 < -0.95$, 70 to -750 Hz) downfield/upfield from the carrier frequency was achieved. The centre of the transition band ($M_z = 0$) was placed at the carrier frequency offset by +60 Hz and -60 Hz for downfield and upfield, respectively. Figure 1 shows the proposed pulse sequence (adiabatic pulse parameters: hyperbolic secant pulse, $HS_{1/2}$, with $R = 10$ and $0.9 \times T_p$, tanh/tan pulse with $R = 40$ and $0.1 \times T_p$).²⁹

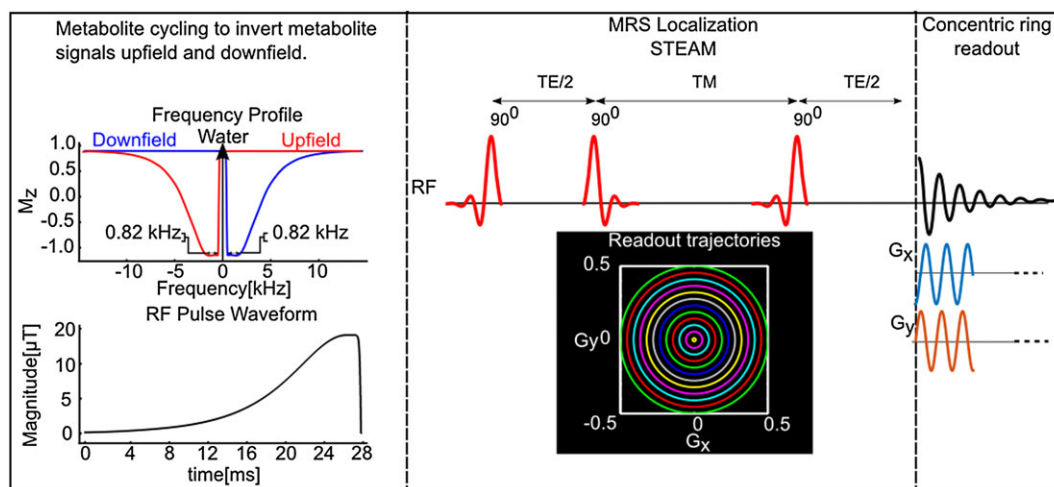


FIGURE 1 Pulse sequence diagram of the proposed MRSI method without water suppression, allowing simultaneous detection of metabolite and water signals by two scans. Prior to a STEAM localization, two asymmetric narrow-transition-band adiabatic RF pulses invert the spectral range where metabolite signals are expected either upfield or downfield with respect to water. Instead of a conventional k -space trajectory, the preparation scheme is followed by a concentric ring k -space trajectory

2.2.2 | Water-suppressed MRSI

For comparison, a water-suppressed MRS acquisition was also made by utilizing an outer volume suppression (OVS) and VAPOR (variable-power RF pulses with optimized relaxation delays) water suppression scheme before the STEAM localization.^{30,31} A Gaussian RF pulse (20.48 ms duration) and crusher gradient (6.6 ms) were used during the mixing time (T_M) period of STEAM to suppress residual water signal in addition to the VAPOR water suppression. Eight RF pulses with variable pulse power and optimized timing were used for VAPOR water suppression. To suppress unwanted signals outside the VOI, OVS pulses were also applied as described in Reference 30.

2.2.3 | In vivo MRSI acquisitions

All *in vivo* 2D MRSI scans from a specific region of interest in the motor cortex were manually positioned using the high-resolution T_1 -weighted MP-RAGE image. STEAM localization ($T_R = 2$ s, $T_E = 14$ ms, $T_M = 32$ ms, number of averages, $N_{avg} = 20$) was used to excite a 65 mm \times 65 mm \times 20 mm region centrally within the field of view (FOV). The imaging box was localized with an FOV of 240 mm \times 240 mm and a slice thickness of 20 mm. The 2D concentric k -space trajectory was used to sample polar k -space data.²³ In order to minimize any reconstruction artefacts for the azimuthally undersampled polar k -space data, the azimuthal sampling criterion, $N_{p,ring} \geq \pi N_{ring}$, was used, where $N_{p,ring}$ is the number of points per ring in the range $0 \leq \theta < 2\pi$ and N_{ring} is the number of rings.³² Thus, 64 points per ring (number of points per ring, $N_{p,ring} = 64$) were collected with an ADC bandwidth of 80 kHz and a maximum slew rate = 67.8 mT/m/ms. 512 temporal points were collected in an effective spectral bandwidth of 1250 Hz. The 64 points per ring were sufficient to satisfy the requirement of avoiding azimuthal aliasing.³² To cover the 24 \times 24 grid in a minimum total acquisition duration, 12 rings (number of rings, $N_{ring} = 12$) resulting in an individual voxel size of 2 mL were acquired in 8 min ($N_{ring} \times N_{avg} \times T_R = 480$ s).²³ This corresponded to a fully excited 6 \times 6 voxel region with a $\frac{1}{2}$ voxel margin outside the STEAM localization.

In order to demonstrate the potential advantages of the non-water-suppressed acquisition scheme for voxel-wise single-scan frequency alignment, as well as phase and eddy current correction, we conducted *in vivo* non-water-suppressed and water-suppressed MRSI measurements from a specific region of interest in the motor cortex with a high in-plane resolution of 5 mm \times 5 mm \times 20 mm ($N_{rings} = 24$, $N_{p,ring} = 64$, FOV = 240 mm \times 240 mm, STEAM localization = 80 mm \times 100 mm \times 20 mm, $T_R = 1.5$ s, $T_E = 14$ ms, $T_M = 32$ ms, $N_{avg} = 20$, ADC bandwidth = 80 kHz, maximum slew rate = 168.2 mT/m/ms, $N_{ring} \times N_{avg} \times T_R = 720$ s) in a healthy subject. In order to simulate frequency changes due to patient motion and long-term magnetic field drift, during *in vivo* MRSI measurements, transmit and receive frequency offsets were varied from 0 Hz to 18 Hz with a 2 Hz increment for every other MRS image. Although this k -space sampling scheme starts to violate the azimuthal sampling criterion at the 20th ring, we did not observe any error in image quality, SNR or resolution (Supporting Figure S1).

2.2.4 | Phantom experiments

The two MRSI sequences were tested on two phantoms. First, the concentric ring k -space trajectory and its reconstruction was tested on a cylindrical resolution phantom (General Electric Medical Systems, Milwaukee, WI, USA) using the non-water suppressed metabolite-cycling MRSI sequence with the following parameters: $N_{rings} = 32$, $N_{p,ring} = 160$, FOV = 320 mm \times 320 mm, STEAM localization = 160 mm \times 160 mm \times 10 mm, $T_R = 2$ s, $T_E = 14$ ms, $T_M = 32$ ms, $N_{avg} = 2$, ADC bandwidth = 200 kHz, maximum gradient slew rate = 141.3 mT/m/ms. The 160 points per ring were sufficient to satisfy the requirement of avoiding azimuthal aliasing.³² Second, a phantom experiment for metabolite spectra depiction for both a water-suppressed and the metabolite-cycling technique was performed on an MRS 'braino' phantom (General Electric Medical Systems, Milwaukee, WI, USA) containing 10 mmol Cr, 3 mmol Cho, 5 mmol lactate (Lac), 1 mL/L Gd-DPTA (Magnevist), 12.5 mmol Glu, 7.5 mmol *myo*-inositol (*myo*-

Ins), 12.5 mmol NAA, 0.1% sodium azide, 56 mmol sodium hydroxide and 50 mmol potassium phosphate monobasic.

2.3 | Post-processing

All the reconstruction algorithms were implemented in MATLAB (MathWorks, Natick, MA, USA). Density compensation was applied to the non-Cartesian k -space data to grid it onto Cartesian k -space,³³ and then a fast Fourier transform (FFT) was performed. Gridding and FFT steps were done by using the non-uniform FFT (NUFFT) toolbox with min-max Kaiser-Bessel kernel interpolation and twofold oversampling.³⁴ The final matrix size of the reconstructed MRSI image after NUFFT was $2N_{\text{ring}} \times 2N_{\text{ring}} \times N_{\text{sp}} \times N_{\text{cha}} \times N_{\text{avg}}$.

2.3.1 | Metabolite-cycling

Odd (upfield) and even (downfield) single-shot non-water-suppressed FIDs edited by the asymmetric RF pulses were frequency and phase corrected on the basis of the water signal. The frequency correction was performed using a cross-correlation algorithm and phase correction was performed using a least-squares fit algorithm. Then, upfield (S_a) and downfield (S_b) edited spectra were summed and used for removing residual eddy current effects,³⁵ combining the phased-array coil spectra³⁶ and metabolite quantification. Metabolite spectra were then calculated by subtraction of alternating FIDs. Potential differences in the water peak amplitude between upfield (S_a) and downfield (S_b) edited spectra were calculated, and then corrected to minimize the residual water peak in the final subtracted metabolite spectrum.¹⁴

$$S_{\text{diff}} = S_a - k \times S_b. \quad (1)$$

The correction factor, k , was determined from the integral of the water peak.

2.3.2 | Water signal calibration for water-suppressed MRSI

An additional unsuppressed water scan was acquired for the water-suppressed MRSI protocol to remove residual eddy current effects³⁵ and to combine the phased-array coil spectra.³⁶ Single-shot metabolite spectra were then frequency and phase corrected prior to averaging over N_{avg} using a cross-correlation and a least-squares fit algorithm, respectively. No additional spatial smoothing was used.

2.3.3 | Metabolite quantification

The averaged metabolite spectrum was quantified using the LCModel package.³⁷ The residual water peak was filtered with the Hankel-Lanczos singular value decomposition (HLSVD) algorithm prior to the LCModel analysis.³⁸ Concentrations were calculated using the unsuppressed water spectrum as an internal reference for *in vivo* data, whereas concentrations were reported relative to Cr for the phantom measurement. The model spectra of alanine (Ala), aspartate (Asp), ascorbate/vitamin C (Asc), glycerophosphocholine (GPC), phosphocholine (PC), Cr, phosphocreatine, GABA, glucose, glutamine (Gln), Glu, glutathione, Lac, *myo*-Ins, NAA, N-acetylaspartylglutamate, phosphoethanolamine (PE), *scyllo*-inositol and taurine were generated based on previously reported chemical shifts and coupling

constants^{39,40} by the GAMMA/PyGAMMA simulation library of VeSPA (Versatile Simulation, Pulses and Analysis) to carry out the density matrix formalism.⁴¹ Simulations were performed using the same RF pulses and sequence timings as those on the 3 T system in use. Eight LCModel-simulated macromolecule resonances were included in the analysis at the following positions: 0.91, 1.21, 1.43, 1.67, 1.95, 2.08, 2.25 and 3 ppm.⁴² Concentrations were not corrected for T_1 and T_2 effects or cerebrospinal fluid contribution. If the correlation between two metabolites was consistently high (correlation coefficient < -0.3) in a given region, their sum was reported, e.g. total creatine (Cr + PCr, tCr), total choline (GPC + PC, tCho) and Glu + Gln.

2.3.4 | Bland-Altman analysis

To evaluate any discrepancies between non-water-suppressed and water-suppressed techniques and the limits of agreement, a Bland-Altman analysis⁴³ was performed on those brain metabolites that had Cramér-Rao lower bound (CRLB) goodness of fit values smaller than 20% (total N-acetylaspartate (tNAA), tCr, tCho, *myo*-Ins and Glu + Gln). For each subject and each reported metabolite in the voxels within the STEAM localization (a grid of 6×6), the difference (in $\mu\text{mol/g}$) between the two techniques was calculated. Assuming that the differences between techniques are approximately normally distributed, 95% of the differences will fall between plus or minus 1.96 standard deviations (SD) of the mean difference (the limits of agreement or Bland-Altman reproducibility coefficient).

3 | RESULTS

3.1 | Phantom measurements

Figure 2 shows the results from the resolution phantom for the non-water-suppressed metabolite-cycling MRSI technique, as well as the concentric ring k -space trajectory used, along with the resulting k -space data. Figure 2C shows the conventional MP-RAGE image, and Figure 2D demonstrates the image derived from the MRSI data. Although the final resolution of the image generated from the first time point of the FID was poorer than the MP-RAGE image (0.25 mL versus 0.001 mL), the non-water-suppressed metabolite-cycling MRSI and its reconstruction generated a spectroscopic image with structural information similar to that of MP-RAGE.

Figure 3 shows results from the brain phantom. Spectra from a 6×6 grid localized by non-water-suppressed metabolite-cycling MRSI (Figure 3C) were acquired using the concentric k -space trajectory (Figure 3A,B). Water spectra of 36 localized voxels of odd and even scans for non-water-suppressed metabolite-cycling MRSI are shown in Figure 3D. The correction factor, k , was typically between 1.0007 and 1.0029 for phantom experiments, resulting in a negligible SNR loss.¹⁴ The upfield spectra edited by the asymmetric RF pulses are highlighted as a subfigure in Figure 3D. An overlaid comparison of representative upfield and downfield spectra acquired by non-water-suppressed and water-suppressed methods is illustrated in Figure 3E,F, respectively. Qualitatively, the spectra match up well. Table 1 gives a quantitative comparison of the two methods listing SNR, estimated LCModel metabolite concentrations and Bland-Altman reproducibility

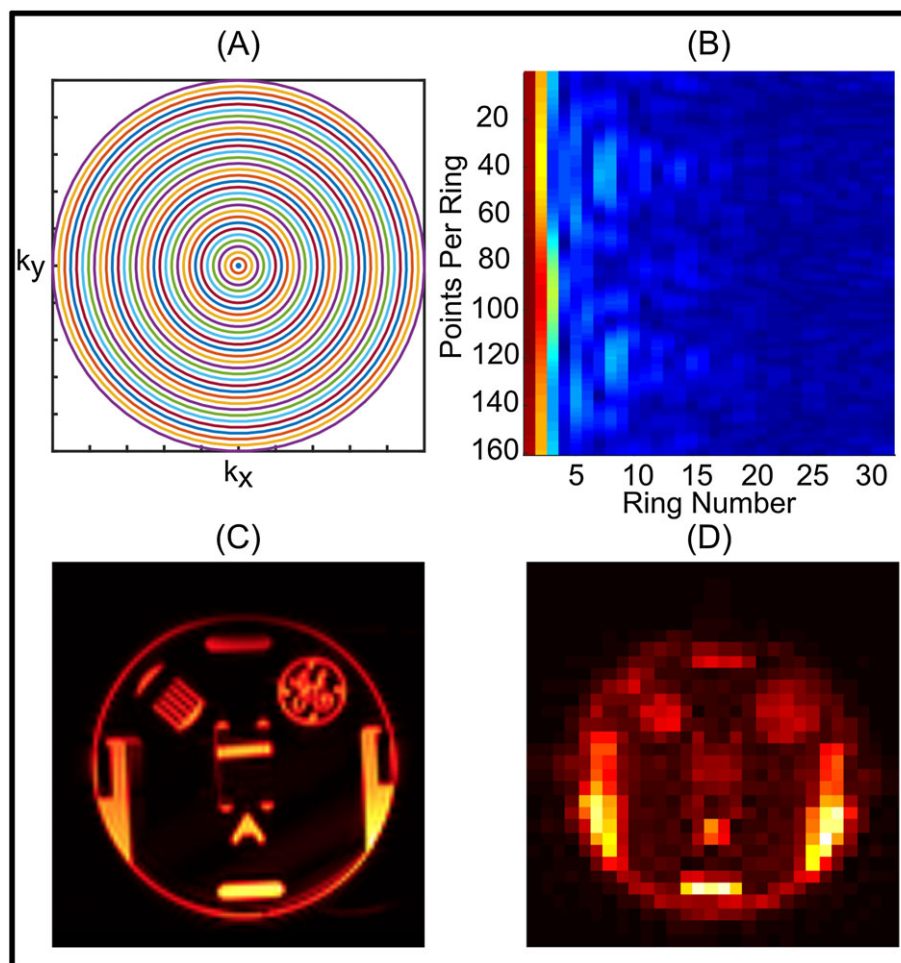


FIGURE 2 A, Concentric ring k -space trajectory used for the resolution phantom experiment. B, k -space data acquired using non-water-suppressed metabolite-cycling MRSI. C, High-resolution T_1 -weighted MPRAGE image of the slice studied. D, Water image with a final grid of 64×64 ($2N_{\text{ring}} \times 2N_{\text{ring}}$) obtained using the first time point of the water FID

coefficient. Quantitative analysis of both methods using the ratio of tNAA, Cho, *myo*-Ins and Lac with respect to Cr resulted in values similar to the specification of the braino phantom.⁴⁴ A strong positive correlation ($r^2 > 0.95$, $p < 0.01$) between concentrations obtained from non-water-suppressed and water-suppressed MRSI was found (36 voxels and five metabolites) (Supporting Figure S2). The mean difference in the estimated concentration across metabolites had a small positive bias (mean \pm SD, 0.035 ± 0.88). The confidence intervals in the limits of agreement defined as the mean concentration/reproducibility coefficient for tNAA (13%), *myo*-Ins (19%) and Cho (15%) were less than those of Glu (24%) and Lac (32%).

Figure 4 illustrates *in vivo* MRSI results from a volunteer. The correction factor, k , was typically between 1.015 and 1.058 in the localized voxels for *in vivo* measurement, resulting in a negligible SNR loss of less than 0.05% (Figure 4A).¹⁴ As shown in Figure 4B,C, reasonable agreement was found between the spectra from non-water-suppressed and water-suppressed MRSI spectra in the range from 1.8 to 4.2 ppm in 36 localized voxels (as indicated at the top left of Figure 4B). An overlaid comparison of representative downfield and upfield spectra acquired by non-water-suppressed and water-suppressed methods is illustrated in Figure 4C,D.

Figure 5A shows the results across all five subjects of quantification with LCModel. Due to the high spectral quality provided by both

techniques, five important brain metabolites could be mapped for all subjects with CRLBs less than 20%. The goodness of the LCModel fit of these metabolites is further visualized by the CRLB maps (Figure 5B) shown for all subjects. CRLB and metabolite maps are complementary to each other for both methods; metabolites with low concentrations (Figure 5A) showed high CRLBs (Figure 5B).

The degree to which the two techniques were in agreement was determined by linear regression analysis. A strong positive correlation ($r^2 > 0.91$, $p < 0.01$) between concentrations obtained from non-water-suppressed and water-suppressed MRSI was found for five brain metabolites for all subjects (36 voxels and five metabolites) (Figure 6). Although the slope of the regression line was very close to unity (mean slope across all subjects $= 0.93 \pm 0.01$), the metabolite concentration estimated using the non-water-suppressed metabolite-cycling MRSI method resulted in slightly higher concentrations. To characterize this bias in more detail, the agreement between the non-water-suppressed and water-suppressed methods was analysed using a Bland-Altman analysis to plot the difference between the two measurements versus their mean (Figure 7). The mean difference of the tNAA across all subjects had a small positive bias (mean \pm SD, 0.16 ± 0.44) whereas the mean difference of tCr, Glu + Gln, tCho and *myo*-Ins had negative biases (-0.33 ± 0.34 , -0.76 ± 0.33 , -0.06 ± 0.05 and -0.05 ± 0.22 , respectively). The confidence intervals

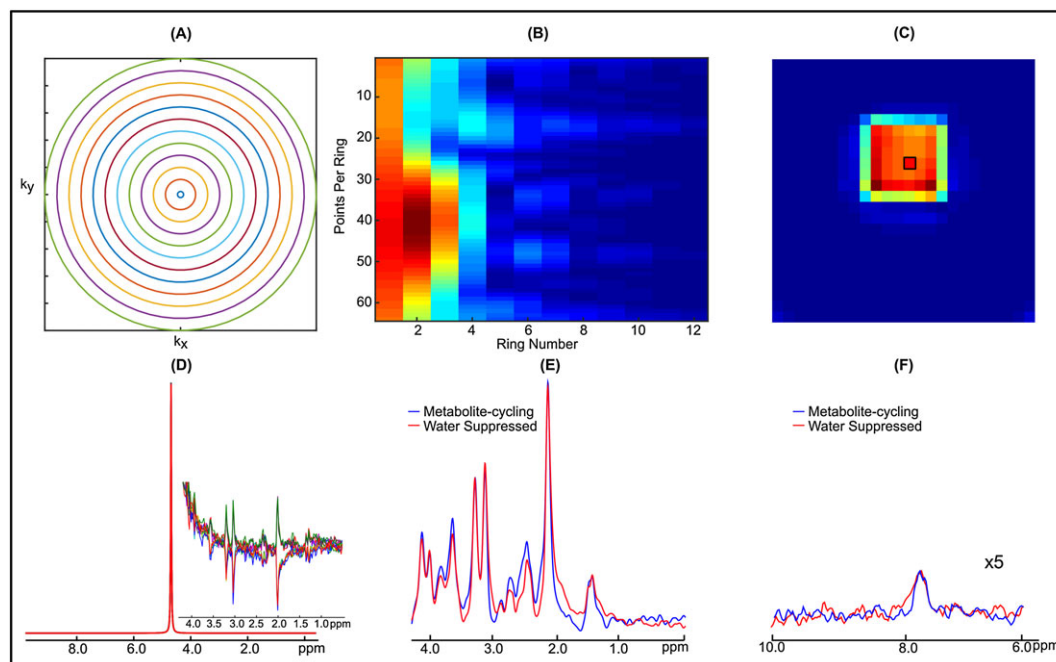


FIGURE 3 A, Concentric ring k -space trajectory used for the brain phantom. B, k -space data acquired using non-water suppressed metabolite-cycling MRSI with following parameters: $N_{\text{ring}} = 12$, $N_{p,\text{ring}} = 64$, FOV = 240 mm \times 240 mm, STEAM localization = 65 mm \times 65 mm \times 20 mm, $T_R = 2$ s, $T_E = 14$ ms, $T_M = 32$ ms, ADC bandwidth = 80 kHz, $N_{\text{avg}} = 10$ and maximum slew rate = 67.8 mT/m/ms. C, Water image with a final grid of 24 \times 24 ($2N_{\text{ring}} \times 2N_{\text{ring}}$) obtained using the first time point of the water FID. D, Spectra of 10 non-water-suppressed water peaks from a voxel taken from the STEAM localized region (black box in C). The subfigure illustrates the effect of asymmetric RF pulses on the upfield spectrum. E, F, Representations of upfield (E) and downfield (F) spectra extracted from a 2 mL voxel (black box in C) from the data acquired using non-water-suppressed (blue) and water-suppressed (red) STEAM localization. The residual water peak was filtered with the HLSVD algorithm. Phantom spectra were line broadened (6 Hz) to match line widths encountered *in vivo*

TABLE 1 Bland–Altman statistics for phantom measurements. Mean metabolite concentration ratios with respect to Cr and Bland–Altman reproducibility coefficient of non-water-suppressed and water-suppressed acquisition schemes (mmol) measured using the Bland–Altman method. SNR, the maximum peak-height divided by the root mean square of residual noise, was calculated using LCModel

	Mean Concentration, Reproducibility Coefficient (mmol)	Phantom Concentration (mmol)
tNAA	12.19, 1.60	12.50
Glu	12.20, 2.90	12.50
tCho	3.08, 0.46	3.00
myo-ilns	6.88, 1.30	7.50
Lac	3.938, 1.21	5.00
	Non-Water Suppressed	Water Suppressed
SNR	28.05 \pm 3.46	29.33 \pm 3.26

for the limits of agreement (Table 2) are narrower for tNAA ($14 \pm 2.1\%$ of mean) and tCr ($17.8 \pm 0.4\%$ of mean), and slightly wider for Glu + Gln ($25 \pm 5.5\%$ of mean), tCho ($22.2 \pm 1.1\%$ of mean) and myo-Ins ($22.8 \pm 2.7\%$ of mean). SNR and linewidths were no different ($p > 0.05$) between the two methods.

Due to the high SNR water peak in the high-resolution MRSI voxel (~ 0.5 mL), non-water-suppressed metabolite-cycling MRSI successfully detected the frequency changes induced by the transmit and receive frequency offsets (Figure 8A), whereas water-suppressed MRSI could not detect these due to poor SNR. Thus, non-water-suppressed

metabolite-cycling MRSI enables voxel-wise single-scan frequency, phase and eddy current correction of metabolite spectra before averaging (Figure 8B), which resulted in visually discernible improvement in spectral quality as compared with water-suppressed spectra (Figure 8C).

4 | DISCUSSION

This study demonstrates that short- T_E 2D MRSI data can be obtained using both non-water-suppressed metabolite-cycling and water-suppressed techniques in the same measurement time as SV-MRS. We have shown that the non-water-suppressed metabolite-cycling method can produce high-quality spectra similar to those produced by the water-suppressed technique. The metabolite concentration values measured using the short- T_E MRSI for different tissues were consistent with previous literature values (see later). Finally, high-resolution non-water-suppressed metabolite-cycling MRSI (~ 0.5 mL) resulted in a significant improvement in the spectral quality compared with water-suppressed spectra by using the water peak for voxel-wise single-scan frequency, phase and eddy current correction. To our knowledge, this is the first study to have validated the use of non-water-suppressed metabolite-cycling techniques for short- T_E MRSI.

In addition to the reduction of sideband artefacts and eddy currents, it has been shown previously that metabolite-cycling offers improved frequency alignment and phase correction for SV-MRS in voxels where insufficient SNR does not permit correction of single-scan acquisitions.^{14,15} In this study, we utilized metabolite-cycling for

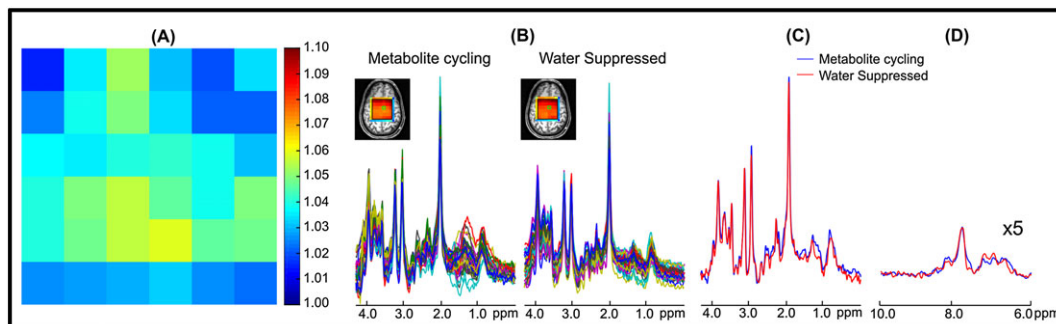


FIGURE 4 A, Spatial distribution of the correction factor, k , in the region of STEAM localization. B, Spectra from localized 6×6 voxels acquired using non-water-suppressed metabolite-cycling and water-suppressed methods without any apodization. Insets show water images overlaid on an anatomical image obtained using the first time point of the water FID. C,D, Representative upfield (C) and downfield (D) spectra are shown extracted from a 2 mL voxel (green box in B). The residual water peak was filtered with the HLSVD algorithm

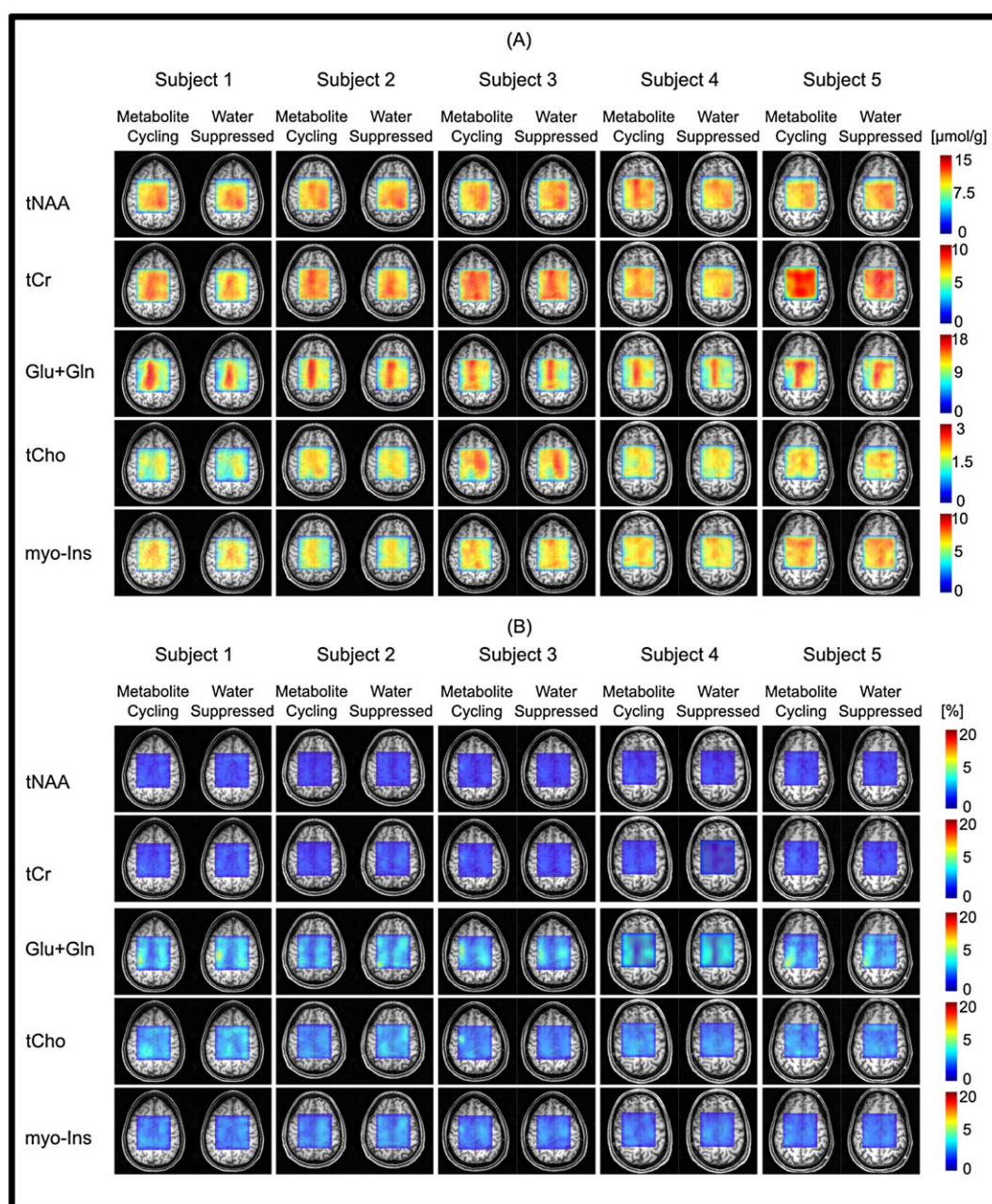


FIGURE 5 Metabolite and CRLB distribution maps obtained from all subjects. Absolute metabolite concentration (A) and CRLB (B) maps of tNAA, tCr, Glu + Gln, tCho and myo-Ins overlaid on an anatomical image

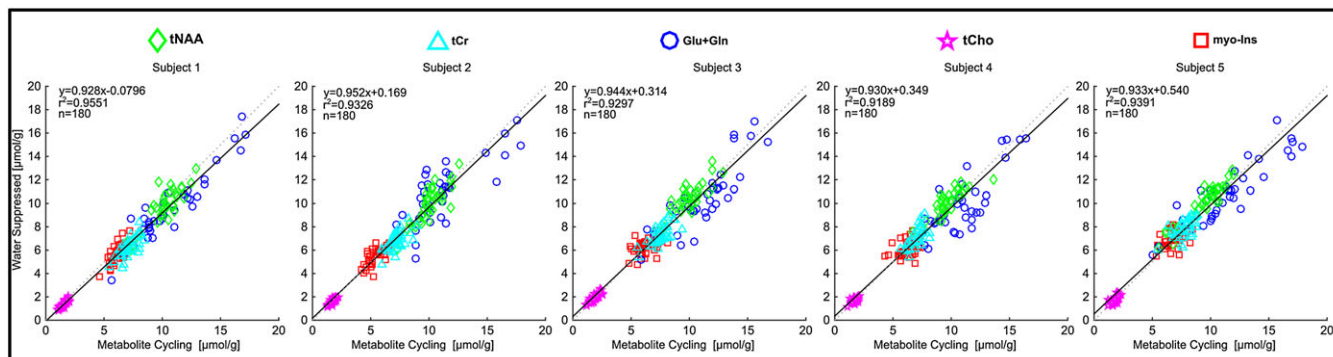


FIGURE 6 Correlation between concentrations quantified from each localized voxel using non-water-suppressed metabolite-cycling and water-suppressed MRSI from all subjects. The dashed (grey) and solid (black) lines represent the unity and linear regression lines, respectively

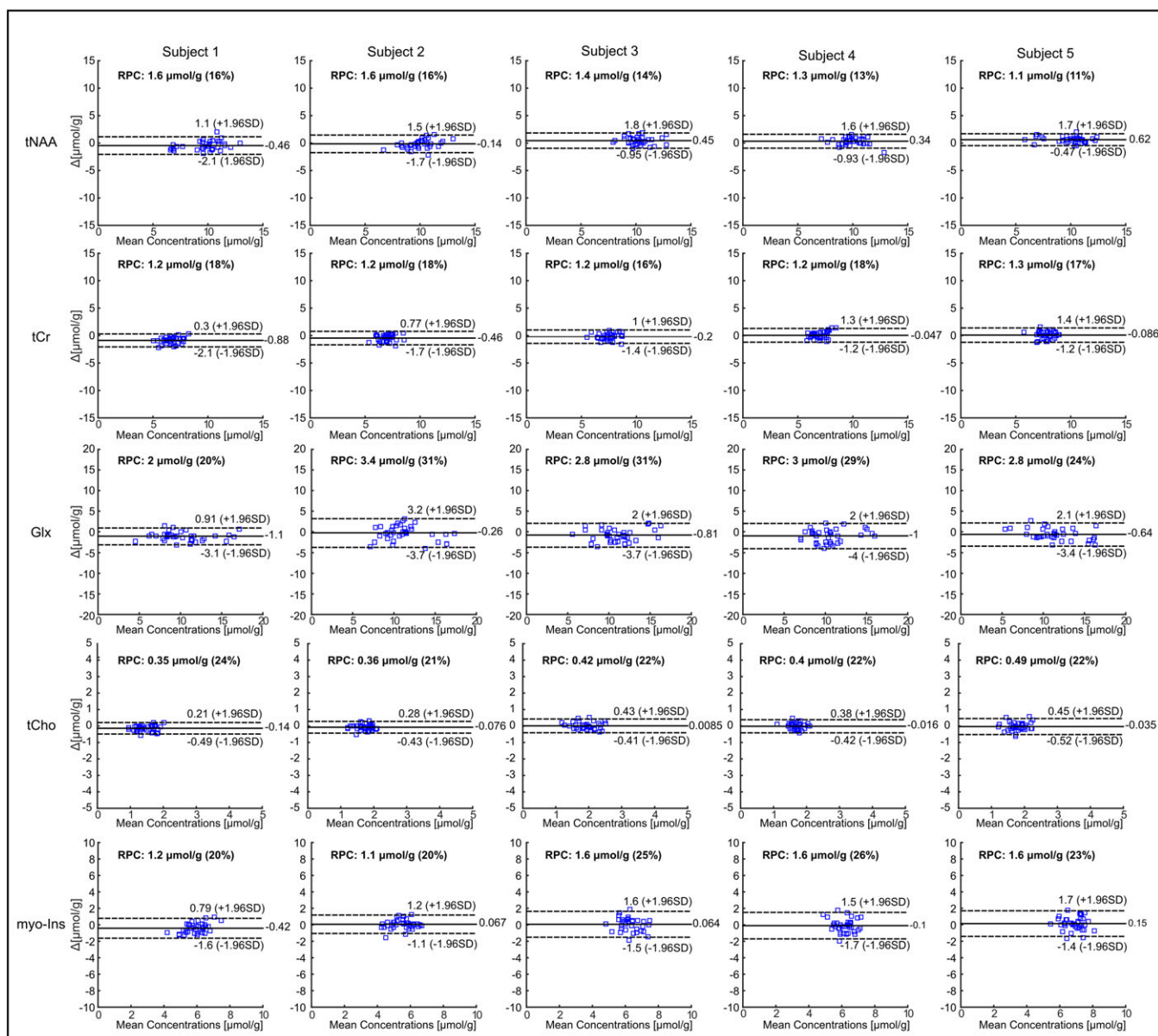


FIGURE 7 Bland-Altman analysis of *in vivo* measurements. Bland-Altman plots indicate the limits of agreement between metabolite concentrations quantified from non-water-suppressed metabolite-cycling and water-suppressed MRSI from each subject. The y-axis shows the difference between the two techniques for each localized voxel (water suppressed – non-water-suppressed, Δ) and the x-axis represents the average of these measures (water suppressed + non-water-suppressed)/2, mean). The dotted lines represent ±1.96 SD with the limits of agreement. The solid line represents the mean bias

TABLE 2 Bland–Altman statistics for *in vivo* measurements. Mean absolute metabolite concentration and Bland–Altman reproducibility coefficient of non-water-suppressed and water-suppressed acquisition techniques ($\mu\text{mol/g}$) measured using the Bland–Altman method. LW and SNR were calculated using LCMModel analysis

Mean Concentration, Reproducibility Coefficient ($\mu\text{mol/g}$)	Subject 1		Subject 2		Subject 3		Subject 4		Subject 5	
	Non-Water Suppressed	Water Suppressed	Non-Water Suppressed	Water Suppressed	Non-Water Suppressed	Water Suppressed	Non-Water Suppressed	Water Suppressed	Non-Water Suppressed	Water Suppressed
tNAA	9.80, 1.60	10.00, 1.60	10.00, 1.60	10.00, 1.40	10.00, 1.40	9.90, 1.30	9.90, 1.30	9.90, 1.10	9.90, 1.10	9.90, 1.10
tCr	6.70, 1.20	7.00, 1.20	7.00, 1.20	7.50, 1.20	7.50, 1.20	7.00, 1.20	7.00, 1.20	7.80, 1.30	7.80, 1.30	7.80, 1.30
Glu + Gln	10.00, 2.00	11.00, 3.40	11.00, 3.40	11.00, 2.80	11.00, 2.80	10.00, 3.00	10.00, 3.00	11.00, 2.80	11.00, 2.80	11.00, 2.80
tCho	1.50, 0.35	1.70, 0.36	1.70, 0.36	1.90, 0.42	1.90, 0.42	1.70, 0.40	1.70, 0.40	1.80, 0.49	1.80, 0.49	1.80, 0.49
myo-Ins	6.00, 1.20	5.50, 1.10	5.50, 1.10	6.30, 1.60	6.30, 1.60	6.20, 1.60	6.20, 1.60	6.90, 1.60	6.90, 1.60	6.90, 1.60
Linewidth (Hz)	5.86 \pm 0.90	5.87 \pm 0.75	6.07 \pm 1.06	5.99 \pm 0.96	5.87 \pm 0.86	5.91 \pm -0.74	6.20 \pm 0.83	5.80 \pm 0.79	5.96 \pm 0.98	5.80 \pm 0.93
SNR	24.63 \pm 3.42	23.50 \pm 3.32	27.55 \pm 3.16	21.94 \pm 3.40	26.55 \pm 4.33	29.97 \pm -4.33	27.11 \pm 3.83	29.88 \pm 4.00	24.61 \pm 4.33	26.50 \pm 5.31

the MRSI acquisition within a clinically feasible acquisition time using a concentric ring *k*-space trajectory. This acquisition scheme allowed us to obtain water and metabolite resonances simultaneously without requiring any additional water-suppressed measurements. Similarly to the earlier SV metabolite-cycling studies,^{14,15} the non-water-suppressed spectra were used as an internal reference for quantification of the metabolite signals and as a reference to correct residual eddy currents, coil combination and frequency drifts in the B_0 field due to subject motion and/or hardware instability. The metabolite spectra (subtracted spectra) and estimated concentrations were in agreement with the water-suppressed MRSI acquisitions (Figure 4). Since both non-water-suppressed and water-suppressed MRSI resulted in high spectral quality over the STEAM localization, the single-scan frequency and phase correction were applied for each voxel in the STEAM localization. However, the high-resolution MRSI (~ 0.5 mL), where intrinsic SNR is low, benefited more substantially from the metabolite-cycling technique due to the high SNR of the water signal used for pre-processing steps (Figure 8).

The achieved spectral quality allowed reliable quantification of major brain metabolites with a CRLB of less than 20% using LCMModel analysis. Concentration distributions of metabolites quantified in this study were in good agreement with previously reported values acquired from the same brain locations⁴⁵ and revealed significant variations between different brain tissues (Figure 5). The findings are in agreement with previous MRS studies of the anatomical locations most similar to the regions presented here. For example, Glu + Gln, tCr and myo-Ins showed higher concentrations in the region of grey matter (GM) compared with white matter (WM).^{45–47} The concentration of tNAA had a fairly homogeneous distribution, consistent with previous MRS studies.^{45–47} In addition, we found elevated tCho, specifically tCho/tCr, in WM in comparison with GM.⁴⁸

There remain several limitations of the implemented methods. First, although we used a short gap (9.6 ms) between the STEAM excitation and asymmetric adiabatic RF inversion pulse, the long T_M (32 ms) period of non-water-suppressed metabolite-cycling STEAM MRSI might lead to a magnetization transfer effect on several metabolites.⁴⁹ This can be minimized by incorporating the asymmetric adiabatic RF inversion pulse into the T_M period.¹⁶ Second, metabolite signals closest to the water peak, such as myo-Ins, tCho, Lac and tCr, might be reduced due to imperfections in the chemical-shift-selective RF pulses caused by local magnetic field variability. The asymmetric adiabatic RF inversion pulses used in this study were designed to minimize the effect of local magnetic field variability by placing the centre of the transition band ($M_z = 0$) at the carrier frequency offset by ± 60 Hz. This is further supported by the negative concentration biases of tCr, tCho and myo-Ins (Figure 7), indicating that local magnetic field variability induced more signal loss for the water-suppressed MRSI technique. The signal intensities of these metabolites might be reduced by the water suppression due to magnetization exchange with water.¹⁸ In addition, these negative concentration biases could also be explained by the shortening of T_1 relaxation times in the 1–4 ppm region when non-water-suppressed metabolite-cycling STEAM MRSI is used.⁵⁰ Furthermore, when larger VOIs are studied, for which the B_1 and B_0 fields will be moderately inhomogeneous at 3 T, resulting in imperfect inversion, utilization of

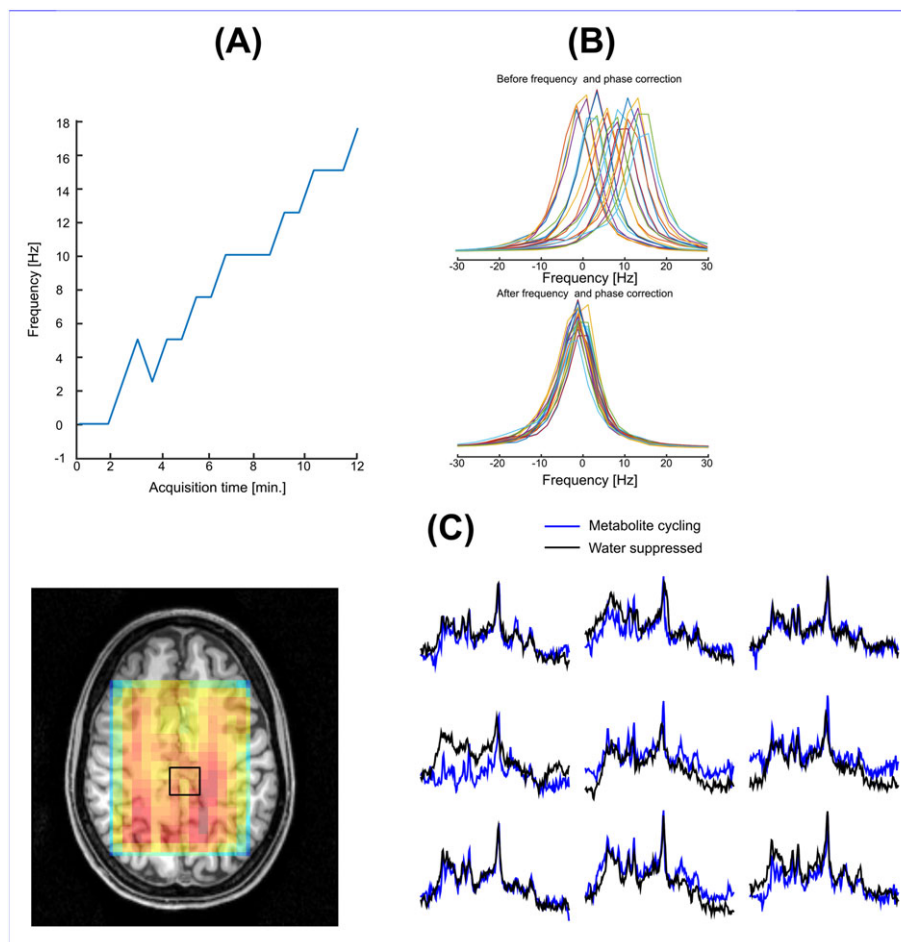


FIGURE 8 A, Water resonance frequency versus acquisition time. In order to simulate frequency changes due to patient motion and long-term magnetic field drift, during *in vivo* MRSI measurements transmit and receive frequency offsets were varied from 0 Hz to 18 Hz with a 2 Hz increment for every other MRS image. B, Spectra of 20 non-water-suppressed water peaks of one volunteer without (top) and with (bottom) frequency alignment and phase correction. C, Spectra from high resolution (5 mm × 5 mm × 20 mm) using non-water-suppressed metabolite-cycling and water-suppressed methods. The inset shows the water image overlaid on an anatomical image

B_1 and higher-order B_0 shimming might help achieve homogeneous B_1 and B_0 over the entire VOI. Another potential limitation of the implemented metabolite-cycling technique was higher lipid contamination due to the omission of the OVS pulses, which affects macromolecule resonances in the 0.5 to 2.0 ppm region (Figure 4). Although the metabolite-cycling technique is a spectral subtraction-based technique and is vulnerable to subject motion or hardware instability leading to subtraction errors, non-water-suppressed MRS images are expected to be used for real-time motion and scanner drift artefact corrections to minimize these errors. Finally, in this study, we chose to utilize STEAM localization with a penalty of twofold signal loss compared with PRESS or semi-LASER since short T_E values can easily be achieved with lower peak RF pulse powers, yielding a lower specific absorption rate (SAR). This is especially important for potential short- T_R high-resolution MRSI studies in humans, where SAR might be a problem.

In conclusion, we have developed and demonstrated a non-water-suppressed metabolite-cycling MRSI technique that performs robustly on clinical MRI scanners. The proposed novel MRSI technique will be beneficial not only for acquiring simultaneous metabolite and internal reference data, but also for providing calibration information for

combining phased-array coil and data for correcting residual eddy currents, as well as phase and frequency drifts. These advancements can easily be extended to whole brain MRSI via advanced post-processing and reconstruction techniques.⁵¹

ACKNOWLEDGEMENTS

The authors would like to acknowledge the following: the Wellcome Trust (UE) and the Dunhill Medical Trust (PJ). The authors acknowledge the scientific support of Dr Jon Furuyama and Dr Neil Wilson in the earlier development of the SI-CONCEPT sequence at the University of California. The authors thank Drs Aaron Hess and Johanna Vannesjo for helpful discussions about frequency drift due to motion and hardware instability.

REFERENCES

- Oz G, Alger JR, Barker PB, et al. Clinical proton MR spectroscopy in central nervous system disorders. *Radiology*. 2014;270(3):658-679.
- Barron HC, Vogels TP, Emir UE, et al. Unmasking latent inhibitory connections in human cortex to reveal dormant cortical memories. *Neuron*. 2016;90(1):191-203.

3. Stagg CJ, Knight S, Talbot K, Jenkinson M, Maudsley AA, Turner MR. Whole-brain magnetic resonance spectroscopic imaging measures are related to disability in ALS. *Neurology*. 2013;80(7):610-615.
4. Emir UE, Tuite PJ, Oz G. Elevated pontine and putamenal GABA levels in mild-moderate Parkinson disease detected by 7 tesla proton MRS. *PLoS One*. 2012;7(1):e30918.
5. Choi C, Ganji SK, DeBerardinis RJ, et al. 2-hydroxyglutarate detection by magnetic resonance spectroscopy in IDH-mutated patients with gliomas. *Nat Med*. 2012;18(4):624-629.
6. Pope WB, Prins RM, Albert Thomas M, et al. Non-invasive detection of 2-hydroxyglutarate and other metabolites in IDH1 mutant glioma patients using magnetic resonance spectroscopy. *J Neurooncol*. 2012;107(1):197-205.
7. Berrington A, Voets NL, Plaha P, et al. Improved localisation for 2-hydroxyglutarate detection at 3 T using long-TE semi-LASER. *Tomography*. 2016;2(2):94-105.
8. Ogg RJ, Kingsley PB, Taylor JS. WET, a T_1 - and B_1 -insensitive water-suppression method for *in vivo* localized ^1H NMR spectroscopy. *J Magn Reson B*. 1994;104(1):1-10.
9. Haase A, Frahm J, Hanicke W, Matthaei D. ^1H NMR chemical shift selective (CHESS) imaging. *Phys Med Biol*. 1985;30(4):341-344.
10. Mescher M, Merkle H, Kirsch J, Garwood M, Gruetter R. Simultaneous *in vivo* spectral editing and water suppression. *NMR Biomed*. 1998;11(6):266-272.
11. Patt SL, Sykes BD. Water eliminated Fourier-transform NMR-spectroscopy. *J Chem Phys*. 1972;56(6):3182-3184.
12. Chadzynski GL, Klose U. Proton CSI without solvent suppression with strongly reduced field gradient related sideband artifacts. *Magn Reson Mater Phys Biol Med*. 2013;26(2):183-192.
13. Dong Z. Proton MRS and MRSI of the brain without water suppression. *Prog Nucl Magn Reson Spectrosc*. 2015;86-87:65-79.
14. Dreher W, Leibfritz D. New method for the simultaneous detection of metabolites and water in localized *in vivo* ^1H nuclear magnetic resonance spectroscopy. *Magn Reson Med*. 2005;54(1):190-195.
15. Hock A, MacMillan EL, Fuchs A, et al. Non-water-suppressed proton MR spectroscopy improves spectral quality in the human spinal cord. *Magn Reson Med*. 2013;69(5):1253-1260.
16. MacMillan EL, Kreis R, Fuchs A, et al. New technique for metabolite cycled non-water-suppressed proton spectroscopy in the human brain at 7 T. *Proc Int Soc Magn Reson Med*. 2011;19:1412.
17. van Der Veen JW, Weinberger DR, Tedeschi G, Frank JA, Duyn JH. Proton MR spectroscopic imaging without water suppression. *Radiology*. 2000;217(1):296-300.
18. MacMillan EL, Chong DG, Dreher W, Henning A, Boesch C, Kreis R. Magnetization exchange with water and T_1 relaxation of the downfield resonances in human brain spectra at 3.0 T. *Magn Reson Med*. 2011;65(5):1239-1246.
19. Mansfield P. Spatial mapping of the chemical shift in NMR. *Magn Reson Med*. 1984;1(3):370-386.
20. Adalsteinsson E, Irarrazabal P, Topp S, Meyer C, Macovski A, Spielman DM. Volumetric spectroscopic imaging with spiral-based k-space trajectories. *Magn Reson Med*. 1998;39(6):889-898.
21. Schirda CV, Tanase C, Boada FE. Rosette spectroscopic imaging: optimal parameters for alias-free, high sensitivity spectroscopic imaging. *J Magn Reson Imaging*. 2009;29(6):1375-1385.
22. Jiang W, Lustig M, Larson PE. Concentric rings K-space trajectory for hyperpolarized ^{13}C MR spectroscopic imaging. *Magn Reson Med*. 2016;75(1):19-31.
23. Furuyama JK, Wilson NE, Thomas MA. Spectroscopic imaging using concentrically circular echo-planar trajectories *in vivo*. *Magn Reson Med*. 2012;67(6):1515-1522.
24. Wu HH, Lee JH, Nishimura DG. Fat/water separation using a concentric rings trajectory. *Magn Reson Med*. 2009;61(3):639-649.
25. Maudsley AA, Domenig C, Govind V, et al. Mapping of brain metabolite distributions by volumetric proton MR spectroscopic imaging (MRSI). *Magn Reson Med*. 2009;61(3):548-559.
26. Otazo R, Mueller B, Ugurbil K, Wald L, Posse S. Signal-to-noise ratio and spectral linewidth improvements between 1.5 and 7 Tesla in proton echo-planar spectroscopic imaging. *Magn Reson Med*. 2006;56(6):1200-1210.
27. Lam F, Ma C, Clifford B, Johnson CL, Liang ZP. High-resolution ^1H -MRSI of the brain using SPICE: data acquisition and image reconstruction. *Magn Reson Med*. 2016;76(4):1059-1070.
28. Shah S, Kellman P, Greiser A, Weale P, Zuehlsdorff S, Jerecic R. Rapid fieldmap estimation for cardiac shimming. *Proc Int Soc Magn Reson Med*. 2009;17:565.
29. Hwang TL, van Zijl PC, Garwood M. Asymmetric adiabatic pulses for NH selection. *J Magn Reson*. 1999;138(1):173-177.
30. Tkac I, Gruetter R. Methodology of ^1H NMR spectroscopy of the human brain at very high magnetic fields. *Appl Magn Reson*. 2005;29(1):139-157.
31. Emir UE, Auerbach EJ, Van De Moortele PF, et al. Regional neurochemical profiles in the human brain measured by ^1H MRS at 7 T using local B_1 shimming. *NMR Biomed*. 2012;25(1):152-160.
32. Lauzon ML, Rutt BK. Polar sampling in k-space: reconstruction effects. *Magn Reson Med*. 1998;40(5):769-782.
33. Pipe JG, Menon P. Sampling density compensation in MRI: rationale and an iterative numerical solution. *Magn Reson Med*. 1999;41(1):179-186.
34. Fessler JA, Sutton BP. Nonuniform fast Fourier transforms using min-max interpolation. *IEEE Trans Signal Process*. 2003;51(2):560-574.
35. Klose U. *In vivo* proton spectroscopy in presence of eddy currents. *Magn Reson Med*. 1990;14(1):26-30.
36. Walsh DO, Gmitro AF, Marcellin MW. Adaptive reconstruction of phased array MR imagery. *Magn Reson Med*. 2000;43(5):682-690.
37. Provencher SW. Automatic quantitation of localized *in vivo* ^1H spectra with LCModel. *NMR Biomed*. 2001;14(4):260-264.
38. Cabanes E, Confort-Gouny S, Le Fur Y, Simond G, Cozzzone PJ. Optimization of residual water signal removal by HLSVD on simulated short echo time proton MR spectra of the human brain. *J Magn Reson*. 2001;150(2):116-125.
39. Govindaraju V, Young K, Maudsley AA. Proton NMR chemical shifts and coupling constants for brain metabolites. *NMR Biomed*. 2000;13(3):129-153.
40. Tkac I. Refinement of simulated basis set for LCModel analysis. *Proc Int Soc Magn Reson Med*. 2008;16:1624.
41. Soher BJ, Semanchuk P, Todd D, Steinberg J, Young K. VeSPA: integrated applications for RF pulse design, spectral simulation and MRS data analysis. *Proc Int Soc Magn Reson Med*. 2011;19:1410.
42. Schaller B, Xin L, Cudalbu C, Gruetter R. Quantification of the neurochemical profile using simulated macromolecule resonances at 3 T. *NMR Biomed*. 2013;26(5):593-599.
43. Bland JM, Altman DG. Measuring agreement in method comparison studies. *Stat Methods Med Res*. 1999;8(2):135-160.
44. Lattanzi R, Grant AK, Polimeni JR, et al. Performance evaluation of a 32-element head array with respect to the ultimate intrinsic SNR. *NMR Biomed*. 2010;23(2):142-151.
45. Wijnen JP, van Asten JJ, Klomp DW, et al. Short echo time ^1H MRSI of the human brain at 3 T with adiabatic slice-selective refocusing pulses; reproducibility and variance in a dual center setting. *J Magn Reson Imaging*. 2010;31(1):61-70.
46. Henning A, Fuchs A, Murdoch JB, Boesiger P. Slice-selective FID acquisition, localized by outer volume suppression (FIDLOVS) for ^1H -MRSI of the human brain at 7 T with minimal signal loss. *NMR Biomed*. 2009;22(7):683-696.

47. Posse S, Otazo R, Caprihan A, et al. Proton echo-planar spectroscopic imaging of *J*-coupled resonances in human brain at 3 and 4 Tesla. *Magn Reson Med*. 2007;58(2):236-244.
48. Doelken MT, Mennecke A, Stadlbauer A, et al. Multi-voxel magnetic resonance spectroscopy of cerebral metabolites in healthy adults at 3 Tesla. *Acad Radiol*. 2009;16(12):1493-1501.
49. Leibfritz D, Dreher W. Magnetization transfer MRS. *NMR Biomed*. 2001;14(2):65-76.
50. Shemesh N, Dumez JN, Frydman L. Longitudinal relaxation enhancement in ^1H NMR spectroscopy of tissue metabolites via spectrally selective excitation. *Chemistry*. 2013;19(39):13002-13008.
51. Bilgic B, Chatnuntawech I, Fan AP, et al. Fast image reconstruction with L2-regularization. *J Magn Reson Imaging*. 2014;40(1):181-191.

SUPPORTING INFORMATION

Additional Supporting Information may be found online in the supporting information tab for this article.

How to cite this article: Emir UE, Burns B, Chiew M, Jeppard P, Thomas MA. Non-water-suppressed short-echo-time magnetic resonance spectroscopic imaging using a concentric ring *k*-space trajectory. *NMR in Biomedicine*. 2017;e3714. <https://doi.org/10.1002/nbm.3714>